Bulletin of the Earthquake
Research Institute
Vol. 53 (1978), pp. 339-357

13. Crustal Deformation Associated with a Fault Formation Estimated by the Finite Element Method.

By Junzo KASAHARA,

Earthquake Research Institute.

(Received April 21, 1978.)

Abstract

Crustal deformations associated with fault formation are calculated by the finite element method. Four dip angles are considered: (1) vertical; (2) 45 degrees; (3) 26.7 degrees; and (4) horizontal. A low elasticity area is hypothesized as a fault zone. Sets of double couple forces are applied for a fault. Effects due to several variables (boundary condition, fault thickness, fault length and fault depth) are examined, and surface deformations are calculated. Boundary conditions affect the magnitude of surface deformation; depth, length and thickness of a fault affect not only the magnitude, but also the pattern of deformation. For two cases, displacement field and stress field are shown. Using comparisons of the above crustal deformations and field data in the Mikawa earthquake of 1945 (M=7.1), a best-fit model for fault parameters is obtained. The model is in fairly good agreement with that obtained by Ando's dislocation model.

1. Introduction

The physical process for most shallow and intermediate focal depth earthquakes is fairly well interpreted by the dislocation model. On the assumption of the double-couple force, physical parameters for this process have been obtained by using geophysical information such as seismic body wave, seismic surface wave, crustal deformation, aftershock area, and tsunami data. Some investigators (KANAMORI and ANDO, 1973; ANDO, 1974; ABE, 1976) have achieved good results using all the above data.

In the present study, the relationship between fault parameters (seismic source parameters) and crustal deformation is examined using the finite-element method (see, e.g., ZIENKIEWICZ, 1971). When geodetic and sea level data are compared with a calculated crustal deformation, the most reasonable best-fit fault model is obtained. The estimation of tsunami waves using crustal deformation also results in fault parameters. From land-based geodetic stations, it is difficult to detect the crustal deformation resulting from a large earthquake occuring at distant ocean bottoms. If

the focal depth of that earthquake is shallow, tsunami waves might be generated. Using tsunami wave data, we can estimate crustal deformation at the ocean bottom (e.g., AIDA, 1969). Therefore, we can determine fault parameters.

The calculations of crustal deformation associated with dislocation have been carried out by MARUYAMA's (1964) theory and the method of MANSHINHA and SYMLIE (1971) (SAVAGE and HASTIE, 1966, 1969; PLAKER and SAVAGE, 1970; HASTIE and SAVAGE, 1970; FITCH and SCHOLZ, 1971; ANDO, 1971, 1974). On the other hand, SHIMAZAKI (1974) used the finite-element method. Although the finite-element method can be applied to complex boundary models and complex crustal structures, the calculation in three dimensions is difficult if the computer used does not have a large enough memory.

The finite-element method represents a continuous body with finite number of rigid elements (e.g., triangle) divided by imaginary boundaries. The rigid elements are connected at each nodal point to adjacent elements. Since each element is assumed to be rigid, stress and strain distributions in the element are uniform. Based on the assumption of continuation of force and displacement at each node, the stress and displacement in the system composed of all elements are determined under applied force or load and appropriate boundary conditions (see, ZIENKIEWICZ, 1971). This method has been mostly used in civil engineering, structural mechanics, and architecture; the geophysical applications are few (STEPHANSON and BERNER, 1971; LYSMER and DRAKE, 1972; SHIMAZAKI, 1974).

Using given displacements at one side of a fault boundary, SHIMAZAKI (1974) estimated a surface deformation. In the present study, double-couple forces are applied along a fault as a given boundary condition. It is assumed that a fault zone is composed of material with lower elasticity than the surroundings. Slip motion appears along the fault zone because of low-elasticity. Displacement field and stress field are calculated for faults with various dip angles. Fault formation is assumed to be equivalent to earthquake generation. The general features are discussed in the present study; stress drop, moment, and average offset are obtained. The surface deformation is compared with observations and results of other methods in particular cases.

2. Model

For convenience in calculation, four models with different dip angles (θ) are studied: (1) $\theta=90°$, left side up dip-slip (vertical) fault (Model 1, Fig. 1a); (2) $\theta=45°$, reverse dip-slip fault (Model 2, Fig. 1b); (3) $\theta=26.7°$, reverse dip-slip fault (Model 3, Fig. 1c); and (4) $\theta=0°$, horizontal fault

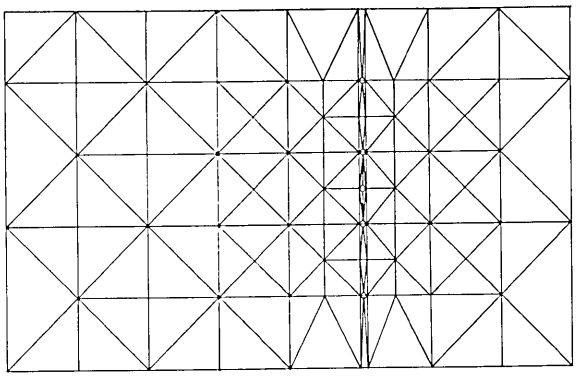

Fig. 1-a

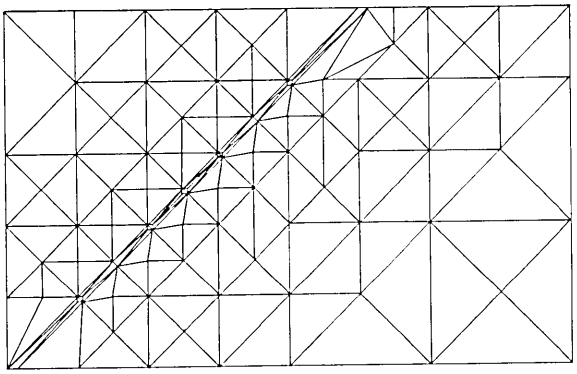

Fig. 1-b

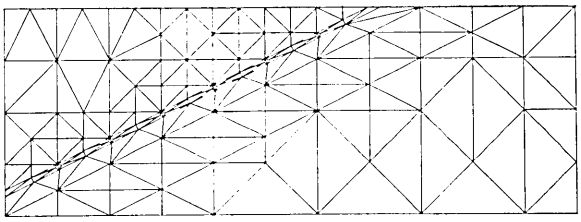

Fig. 1-c

Fig. 1. Models used in the present study with different dip angles: (a) vertical, (b) 45°, and (c) 26.7°. Each triangle unit shows a unit element.

(Model 4, the same structure as Model 1, with different boundary conditions). The parameters and abbreviations used in the text and figures are given in Table 1.

A rectangular area was divided into triangular elements (see Fig. 1). In an element, stress and strain are considered as uniform, and the continuity of stress and strain is held at nodes of one element and its

Table 1. Summary of symbols used in text and figures.

Mo:	Moment (dyne·cm)
Th:	Thickness of fault or distance between two coupled forces (km) (see Fig. 3)
F:	Total applied force (dyne)
f:	Applied force in unit area (dyne/cm^2)
L_1:	Vertical fault length (km) (see Fig. 3)
L_2:	Fault width (km) (see Fig. 3)
d:	Depth of upper end of fault (km) (see Fig. 3)
θ:	Dip angle (degree) (see Fig. 3)
V:	Vertical displacement at the surface (m)
U:	Horizontal displacement at the surface (m)
E_1:	Young's modulus of surrounding material (c.g.s.)
m_1:	Poisson's ratio of surrounding material
E_2:	Young's modulus of fault material (c.g.s.)
m_2:	Poisson's ratio of fault material
$\Delta\sigma$:	Stress drop (bar)
a:	Unit length (km)
S:	Fault area (km^2)$=L_1\times L_2$
D:	Average offset (m)
F:	Free boundary
R:	Rigid boundary
FZ:	Fault zone

adjacent element. A subregion of interest with steep stress variation can be divided into relatively small-sized triangles.

A fault is hypothesized with a layer with lower elasticity than its surroundings. Most of the deformation is concentrated in that low-elasticity layer with thickness, Th. The double couple force is considered an external force. A couple force applies at points P_{01} and P_{02} on both sides of the fault (concentrated forces, F_1 and $-F_1$, Fig. 2a). Another couple force of F_2 and $-F_2$ applies at points of P_{03} and P_{04}. The direction of rotation generated by F_2 and $-F_2$ is counterclockwise. Deformation is produced by the "double couple force". If the layer is composed of material that is of relatively low elasticity and is thin, the layer where the deformation due to the double couple force is concentrated might be considered as a fault zone. The double-couple force applies not only on a set of four points but also on several sets of four points distributed along the fault plane (Fig. 2a). The difference between the effects of a single double-couple force and the effects of distributed double-couple force having the same total forces is small for a fault where $\theta=90°$. The difference, however, is large for the low dip-angle fault. The area where double-couple forces are applied is shown as a dotted zone in the

inserts in the figure showing each result.

The boundary condition is one of the factors which strongly affect the deformation. The rigid right and left boundaries and the free upper boundary are considered in models 1, 2 and 3. Two cases, (1) rigid-and (2) free-bottom boundaries, are considered for model 1, while only the rigid-bottom is considered in models 2 and 3. In model 4, the bottom, left-and right-side boundaries are rigid and the upper boundary is free.

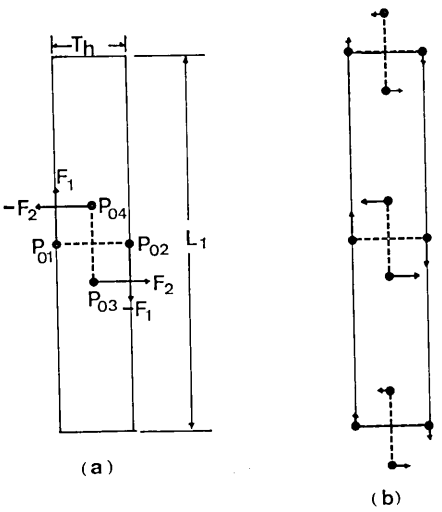

Fig. 2. Schematic representation of (a) a double couple force and (b) 3 sets of double couple force. F_n indicates a force applied on point P_{0n}. Th is the distance between coupled forces and also the thickness of the fault. L_1 is the length of the fault.

In models 1, 2 and 3, Th, L_1, d and the position of the double couple force are varied. In model 4, only d is varied. In most calculations, unit length "a" is chosed as 10 km. Other cases, e.g., $a=100$ km, are estimated by using the results of a case where $a=100$-km. Three different thicknesses (Th) at $a=10$ km, that is, $Th=$ 0.1, 1 and 5 km, are examined in models 1, 2 and 3. Th is 1 km in model 4. The elastic parameters, E and m, are considered as the following: $E_1=6.75\times10^{11}$ c.g.s. and $m_1=0.25$; $E_2=6.75\times10^{9}$ c.g.s. and $m_2=0.40$ for cases where $Th=0.1$ and 1 km; $E_2=3.38\times10^{10}$ c.g.s. and $m_2=0.30$ for the case where $Th=5$ km. For the cases where the fault thicknesses are 0.1 km, 1 km, and 5 km, $F/L_1=10^{14}$ dyne/cm is used. The stress drop ($\Delta\sigma$) is the average stress over the fault zone.

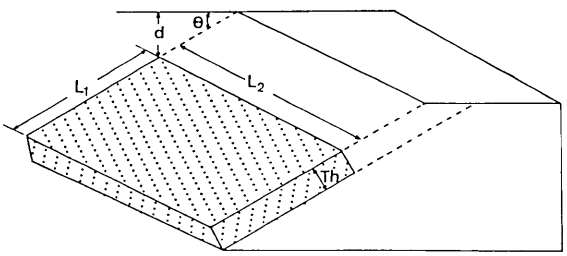

Fig. 3. A fault with a thickness of Th, dip angle of θ, fault dimensions of $L_1\times L_2$ and depth of d.

3. Results

In models 1, 2, and 3 we examine the effects due to the bottom boundary condition, fault thickness (Th), fault depth (d) and vertical length (L_1). In model 4, we examine the depth effect. For convenience in calculation, only, four dip angles ($\theta=90°$, 45°, 26.7° and 0°) were chosen, but the surface deformation at an arbitrary dip angle can be estimated by results of these four models.

(1) *Bottom boundary condition*

Free and rigid-bottom boundary conditions are examined for the vertical fault (model 1). The vertical and horizontal surface deformation (V and U, respectively) is shown in Fig. 4. V and H are not symmetrical due to the different distances from the fault to the right- and left-side boundaries. If the fault is in the center of both boundaries, V and H should be symmetrical. Although the influence of bottom boundary condition change is small for the vertical surface displacement (V) at the right side of the fault and the horizontal surface displacement (U), the bottom boundary condition strongly affects the vertical surface displacement (V) at the left side of the fault. Since the real feature is more likely close to the rigid-bottom boundary condition, the rigid bottom is considered in the other cases.

(2) *Fault thickness (Th) effect*

The fault thickness, Th, strongly affects the surface displacement. Fig. 5 shows the results in the vertical fault (model 1) and the 45° reverse dip-slip fault (model 2). An increase in thickness from 0.1 km to 1 km, results in a five- to ten-times increase in both vertical and horizontal displacements (V and U). Only a slight change is seen in the stress drop ($\Delta\sigma$).

(3) *Fault depth (d) effect*

The depth of the fault (d) strongly affects the surface deformation. In particular, the magnitude and pattern of surface deformation depend upon whether or not a fault reaches the surface. The depth (d) was chosen as 0, 10, and 20 km in model 1 (Fig. 6) and model 2 (Fig. 7). In model 1 (Fig. 6), the displacement near the intersection of a fault (or its extension) and the surface varies with depth changes for both V and U: when a fault reaches the surface, V and U are maxima at the intersection; otherwise, V and U are minima or very small there. In model 2 (Fig. 7), V has the same tendency as the one in model 1. The maximum for U, however, does not occur at the intersection point. U varies

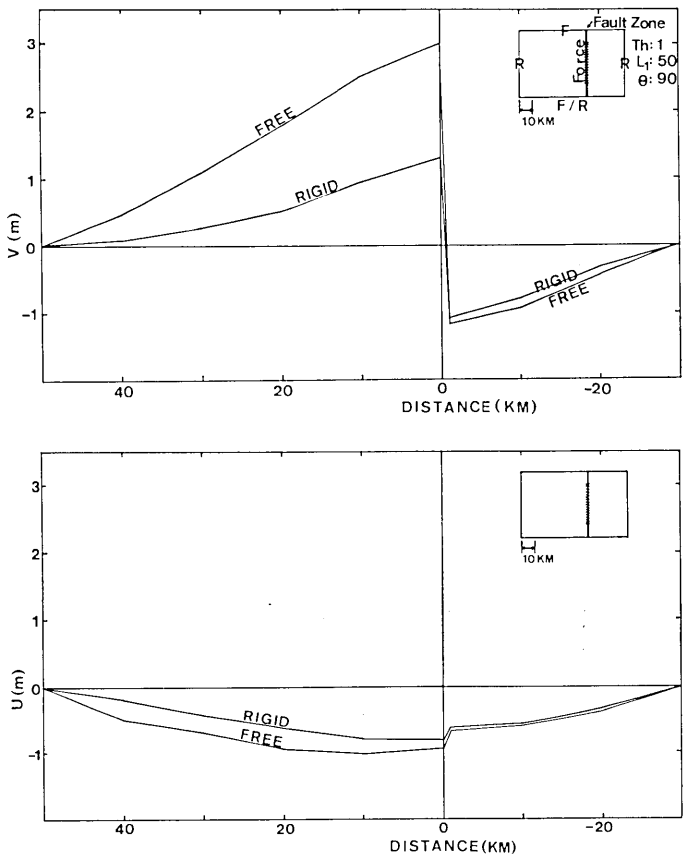

Fig. 4. Boundary condition effect for (a) vertical displacement (V) and (b) horizontal displacement (U) at the surface. Positive sign shows uplift for V and movement to right for U. 0 distance is taken as left side edge of fault for Th=0.1 and 1 km. Models used in calculation are shown as insert figure in upper right. Bottom boundary condition are free or rigid. Right side of insert model shows variables used in calculation. Unit length "a" is shown at bottom of insert model. Fault zone compared with low elasticity material is shown as solid line with dotted zone in each model. Units for variables are km in Th, d and L_1 and degrees in θ. Same notation is used for Figs. 4 to 12 and Fig. 15.

greately around 30-km to the left of the intersection for the depth change from 0 km to 20 km. The maximum V in model 2 occurs around 20-km to the left of the intersection for d=10 km and 20 km.

(4) *Vertical length of fault* (L_1) *effect*

The effects of the vertical length of the fault (L_1) are shown in Fig. 8(Th=5 km, θ=90°), Fig. 9 (Th=1 km, θ=45°), Fig. 10 (Th=5 km, θ=45°), Fig. 11 (Th=1 km, θ=26.7°) and Fig. 12 (Th=5 km, θ=26.7°).

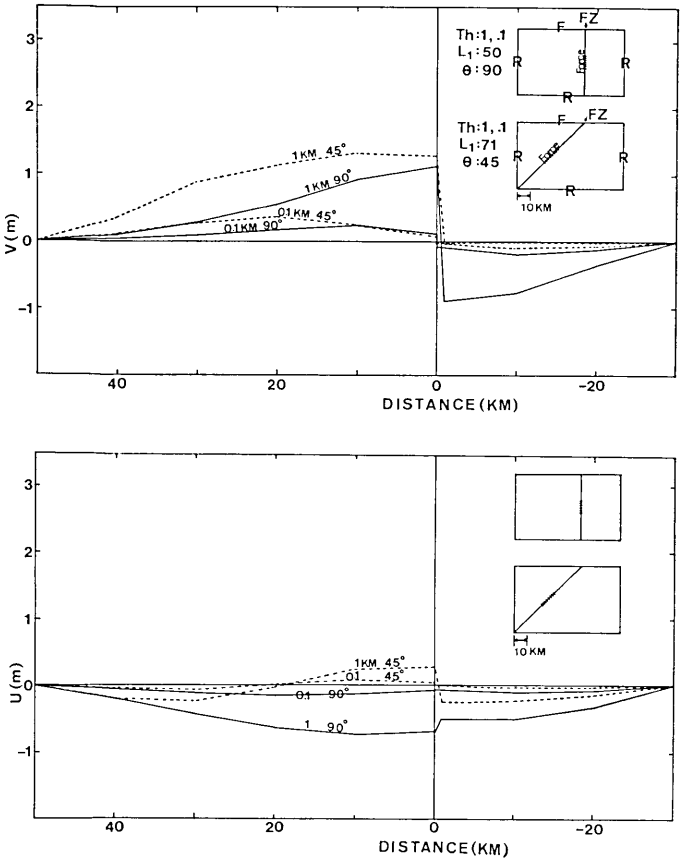

Fig. 5. Fault thickness effect for (a) V and (b) U. V and U for two different thicknesses (0.1 km and 1 km) and two different dip angles (90° and 45°) are calculated. Variables used in calculation are shown on the right-hand side of each model.

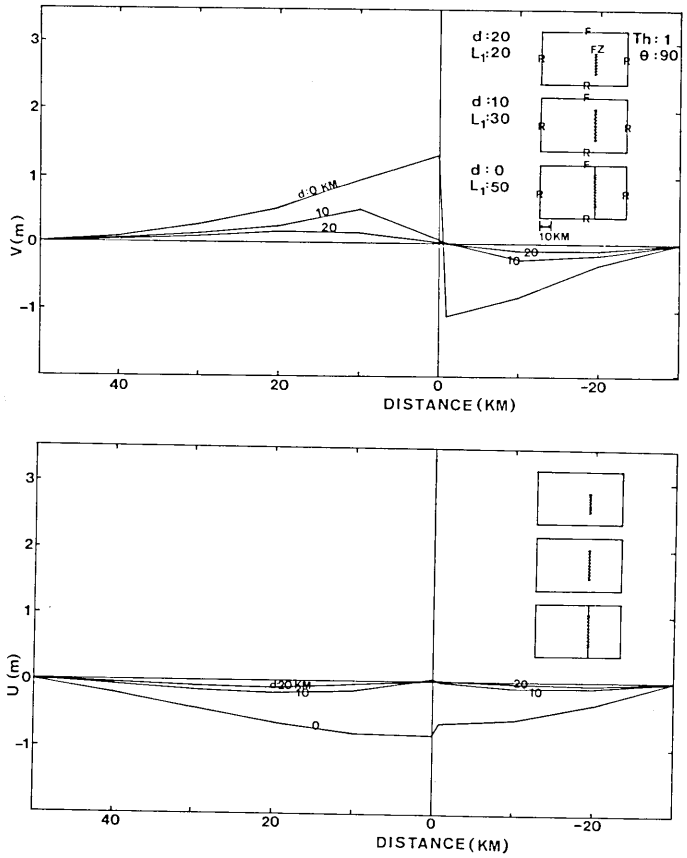

Fig. 6. Depth effect in vertical fault. (a) V and (b) U. Th=1 km. When fault does not reach surface, 0 distance is taken as a cross-point of surface and extension of left edge of fault.

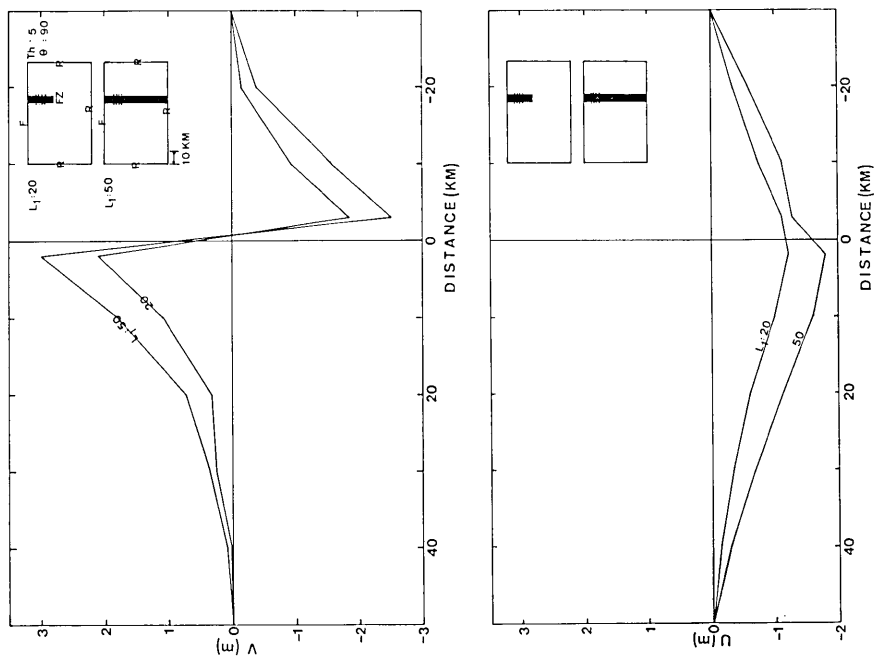

Fig. 8. Vertical length effect in vertical fault with $Th=5$ km. (a) V and (b) U. 0 distance is 2 km right of left edge of fault.

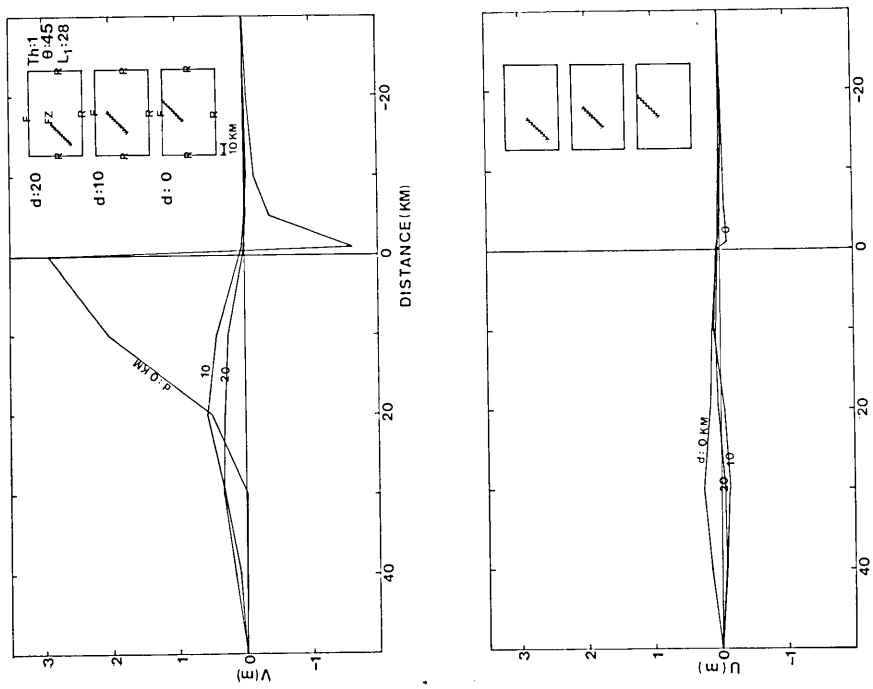

Fig. 7. Depth effect in 45° fault. (a) V and (b) U. $Th=1$ km.

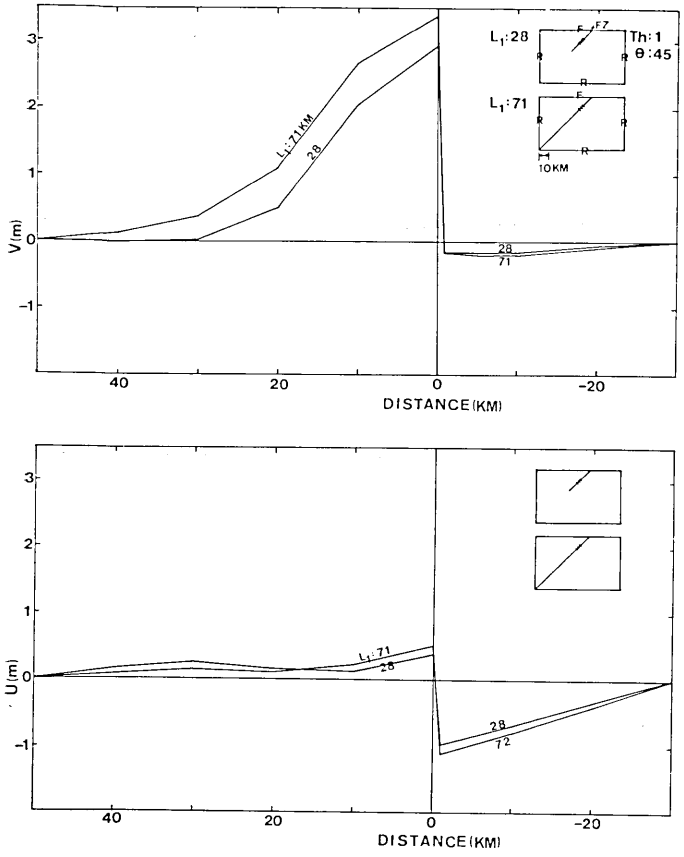

Fig. 9. Vertical length effect in 45° fault with Th=1 km. (a) V and (b) U. Displacement field for the case of L_1=28 km shown in Fig. 13.

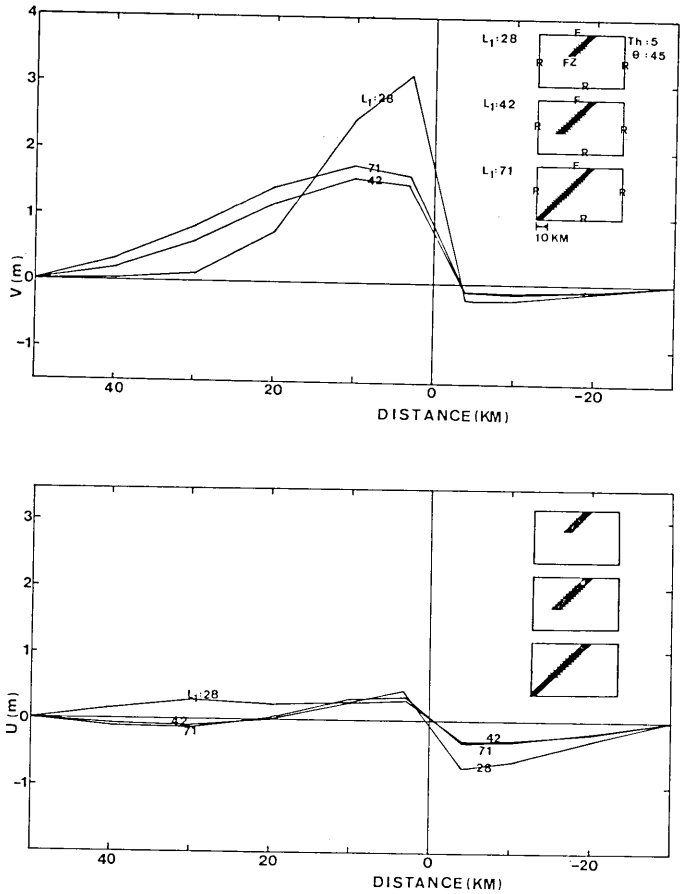

Fig. 10. Vertical length effect in 45° fault with Th=5 km. (a) V and (b) U.

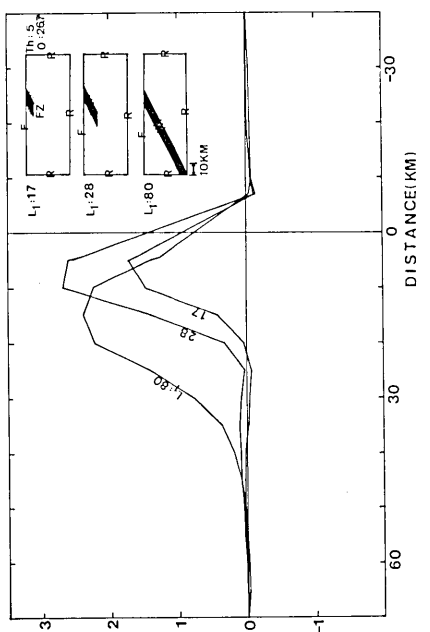

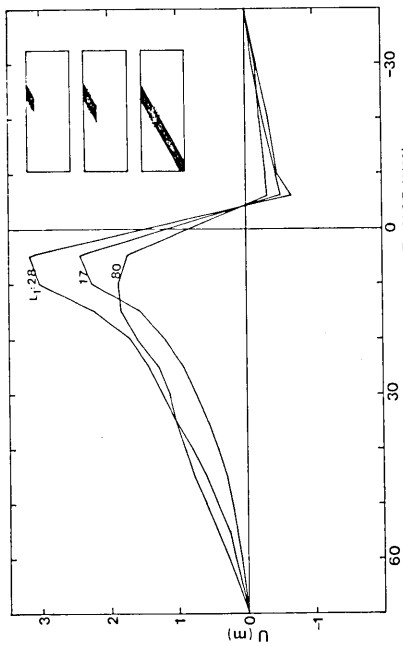

Fig. 12. Vertical length effect in 26.7° fault with $Th=5$ km. (a) V and (b) U. Similar negative values as in the 1 km case shown in Fig. 11a appear in (a), but are smaller than in the 1 km case.

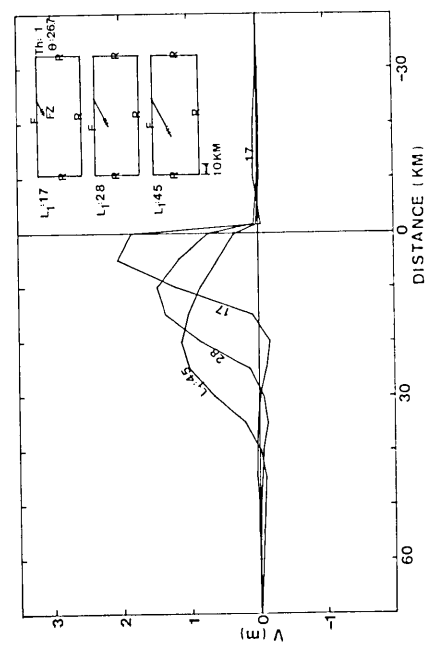

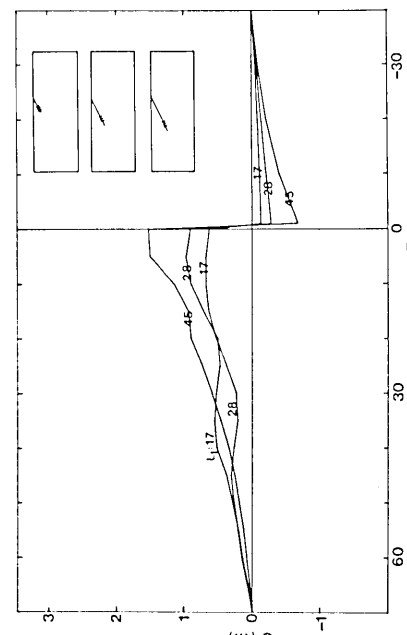

Fig. 11. Vertical length effect in 26.7° fault with $Th=1$ km. (a) V and (b) U. Displacement field and stress field for the case of $L_1=17$ km are shown in Fig. 14. Note that V shows small negative value at left side of fault. Fault with greater dip angle than 26.7° does not show negative value.

The E_2 and m_2 values used in the $Th=5$ km case are different from those in the $Th=0.1$ km and 1 km cases.

For $\theta=90°$ fault (Fig. 8), the fault length L_1 does not change V and U values by a large amount. A 2.5-times change of L_1 changes both V and U from 1.3 to 2 times.

For a $\theta=45°$ fault, on L_1 change does not change V and U by a large amount in the $Th=1$ km case (Fig. 9), but V and U patterns in $L_1=28$ km are different from those in $L_1>28$ km in the $Th=5$ km case (Fig. 10). When $L_1=28$ km, the maximum of V appears around 3-km to the left side of the intersection point, and V sharply decreases with distance. When $L_1>28$ km, the maximum V appears around 10 km, and V gradually decreases. The displacement field for the case of $Th=1$ km, $\theta=45°$ and $L_1=28$ km (see Fig. 9) is illustrated in Fig. 13. The displacement arrows above the fault show approximately the same direction but those below the fault show rotation.

According to the decrease of the dip angle, as seen in the case of $\theta=26.7°$, L_1 effect increases. Note that in the case of $\theta=26.7°$, V is slightly negative at the left side of the intersection (see Figs. 11a and 12a). V is more negative in $Th=1$ km than in $Th=5$ km. The maxima of V in $Th=1$ km and $Th=5$ km occur different places, and the magnitude of the maxima also is different. U variation associated with L_1 variation is not large.

Fig. 14a shows the displacement field for the model where $\theta=26.7°$. This figure corresponds to the case where $L_1=17$ km shown in Fig. 11. The pattern of the stress field (Fig. 14b) is rather complicated. The compression region appears below the fault zone. Although the region above the fault is mainly a zone of tension, the region close to the intersection of the fault and the surface is a zone of compression. At the lower end of the fault zone, the stress is great. This stress concentration may trigger an earthquake. The seismicity induced at a mine in Africa has been reported by McGARR *et al.* (1975). The stress field in Fig 14b is an interpretation of the induced seismicity observed by McGARR *et al.*. Induced mine tremors occurred because the mining hole changed the stress field, resulting in the high shear stress being concentrated at the end of the hole.

(5) *Buried pure horizontal fault (model 4)*

The depth effect is examined for the buried horizontal fault (Fig. 15). When $d=30$ km, the surface deformation is very small. Although the d-variation does not change V and U patterns, it strongly affects the amounts of V and U. V changes from negative to positive above the middle of the fault. U is in the same direction for all cases.

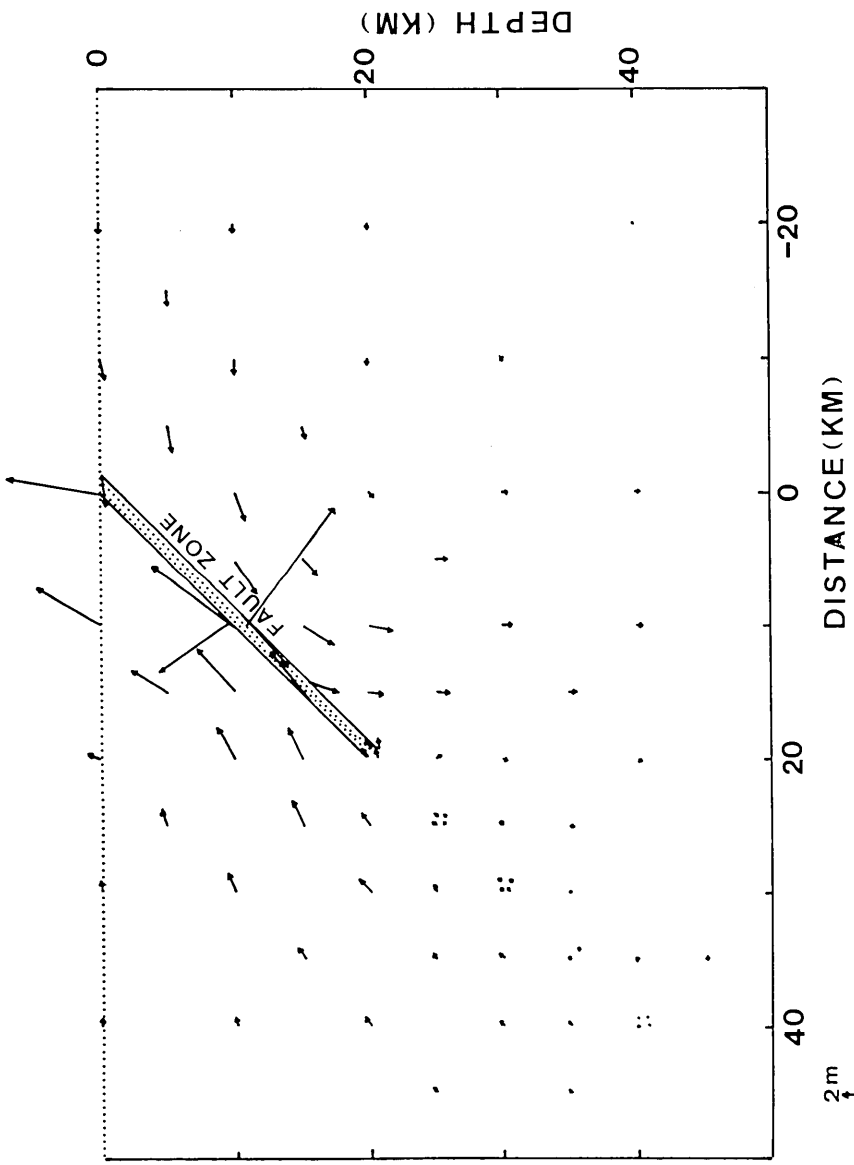

Fig. 13. Displacement field for 45° fault with L_1=28 km and Th=1 km (same as the case in Fig. 9). Arrow shows displacement. Dotted zone shows fault zone. Amplitude scale is shown at left bottom.

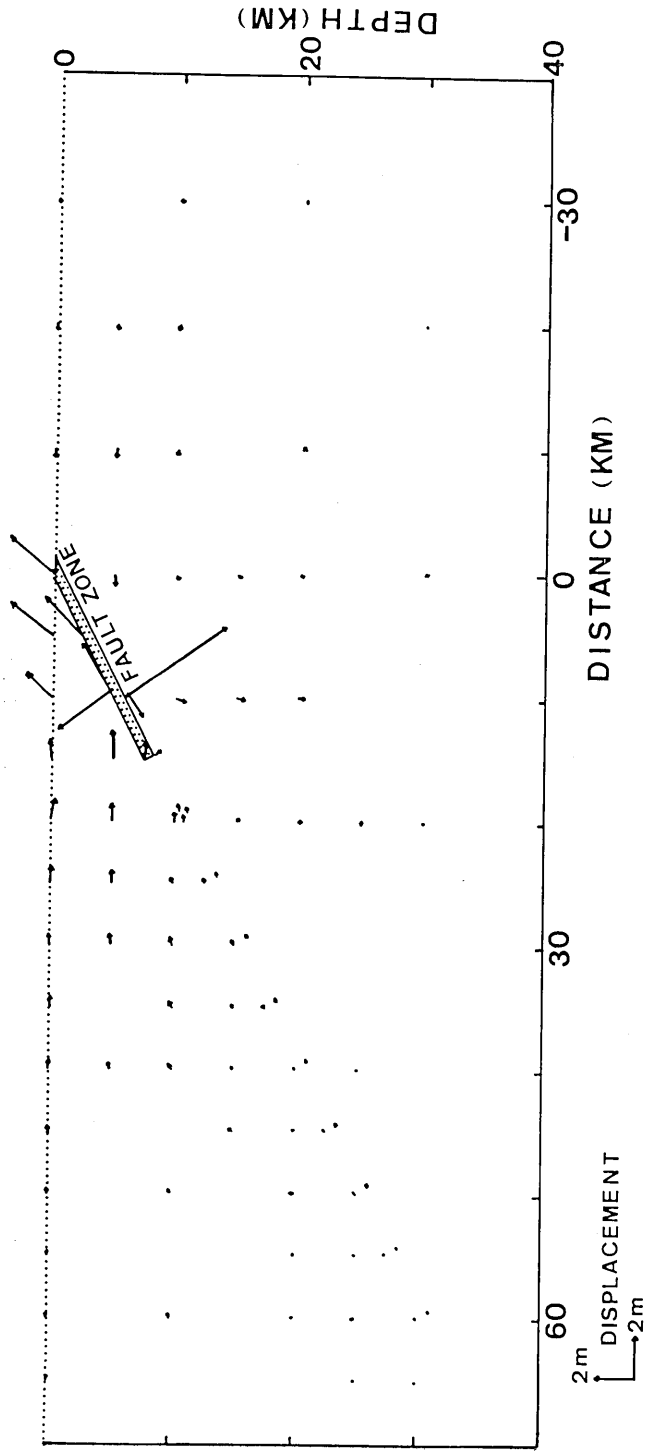
DEPTH (KM)
0
20
40
-30
0
30
60
DISTANCE (KM)
FAULT ZONE
2m
DISPLACEMENT
2m

Fig. 14-a

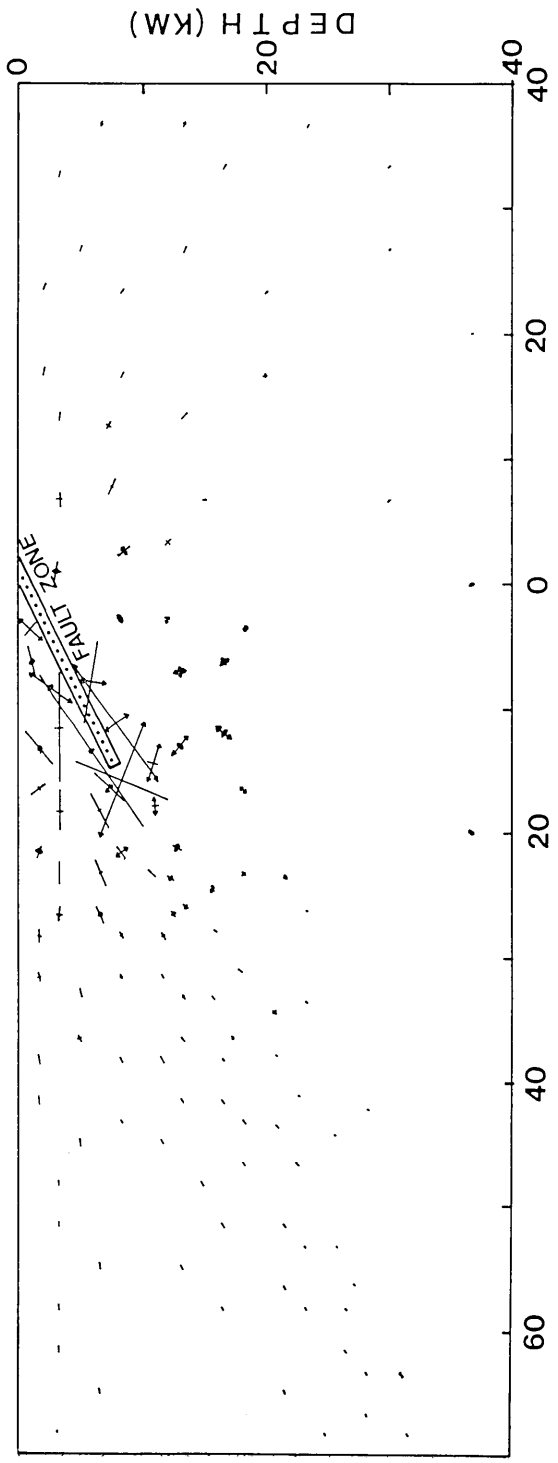

Fig. 14-b

Fig. 14. Displacement field (a) and stress field (b) for 26.7° fault with $L_1=17$ km and $Th=1$ km (same as case in Fig. 11). Stress concentrated at lower end of the fault.

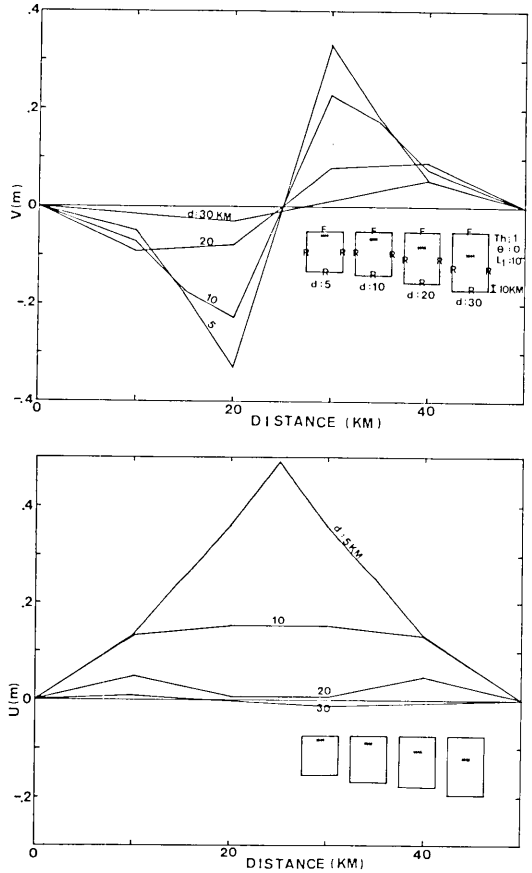

Fig. 15. Pure horizontal fault. (a) V and (b) U. 0 distance is left boundary.

4. Discussion

Other fault parameters—moment, stress drop, fault area, and average offset—can also be calculated by the present models. The average offset, D, is a displacement average over the fault plane. The stress drop ($\Delta\sigma$) is also obtained by the stress averaged over the fault elements. The seismic moment Mo is obtained by the following equation (AKI, 1966)

$$Mo=\mu DS \qquad (1)$$

where μ is rigidity.

ANDO (1974) estimated the source parameters for the MIKAWA earthquake (M=7.1) of 1945, which occurred in central Honshu, Japan. He used the dislocation model and compared his calculation with field data. ANDO's results provide a good test of the reliability of the present method because his study already includes field data and the results of

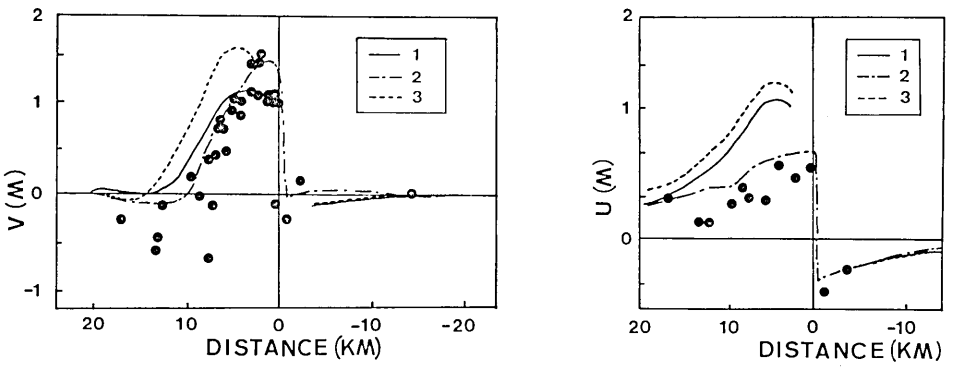

Fig. 16. Comparison of present results with field data of Mikawa earthquake, Japan in 1945 (M=7.1, observation data after ANDO, 1974). (a) V and (b) U. Three models are considered: (1) θ=26.7°, Th=3.25 km and L_1=8.7 km; (2) θ=26.7°, Th=0.65 km and L_1=10.9 km; and (3) θ=26.7°, Th=3.25 km and L_1=14.6 km. Model (2) is in fairly good agreement with observations. Model (2) gives fault parameters listed in Table 2.

Table 2. Comparison of present results and those obtained by dislocation theory (after ANDO, 1974).

	Present Results Case 2	Ando's Results (1974)
Fault size		
Length, L_1 (km)	11	11
Width, L_2 (km)	12 (assumed)	12
Fault thickness, Th (km)	0.67	—
Dip angle, θ (degree)	2.67	30
Moment, Mo (dyne·cm)	6.5×10^{25}	8.7×10^{25}
Stress drop, $\Delta\sigma$ (bar)	76	127
Average offset, D (m)	1.5	2

other methods. Fig. 16 shows the present results for three different models. Circles in Fig. 16 are observations (after ANDO, 1974). Although two models, (1) θ=26.7°, Th=3.25 km, and L_1=8.7 km and (2) θ=26.7°, Th=0.65 km, and L_1=10.9 km, are in agreement with the observed vertical displacement data, case (1) does not satisfy the horizontal displacement data, but case (2) is in agreement with the observations. Case (3), θ=26.7°, Th=3.25 km and L_1=14.6 km, shows slightly larger vertical displacement than the observed values and the horizontal displacement is twice as large as the observed values. ANDO (1974) obtained θ=30°, L_1=11 km, L_2=12 km, and D=2 m. The present results of the dip angle, θ, and the vertical fault length, L_1, agree well with his results. In the present study, L_2 is an undeterminable value because the present calcula-

tion is two-dimensional. We obtained $D=1.5$ m for case (2). This value is close to ANDO's result.

Other fault parameters are obtained (Table 2). The stress drop ($\Delta\sigma$) is about 76 bars for case (2); ANDO (1974) obtained 127 bars. The present stress drop is larger than his $\Delta\sigma$. The moment Mo is 6.5×10^{25} dyne·cm. This moment is approximately the same as ANDO's estimation. As seen in Table 2, the fault parameters agree fairly well with ANDO's estimation except for the stress drop.

We have no measurement of fault thickness, it is possible that the term of fault thickness used in the present study may give a real deformation zone width.

Acknowledgements

The author thanks Professor G. H. SUTTON and E. BERG, University of Hawaii, and Professor T. MARUYAMA, Earthquake Research Institute, University of Tokyo, for their helpful suggestions.

References

ABE, K., 1976, Re-examination of the fault model for the Niigata earthquake of 1964. *J. Phys. Earth*, **23**, 348-366.

AIDA, I., 1969, Numerical experiments for the tsunami propagation—the 1964 Niigata tsunami and the 1968 Tokachi-Oki tsunami. *Bull. Earthq. Res. Inst., Univ. Tokyo*, **47**, 673-700.

AKI, K., 1966, Generation and propagation of G-waves from the Niigata earthquake of June 16, 1964. *Bull. Earthq. Res. Inst., Univ. Tokyo*, **44**, 73-88.

ANDO, M., 1971, A fault-origin model of the great Kanto earthquake of 1923 as deduced from geodetic data. *Bull. Earthq. Res. Inst., Univ. Tokyo*, **49**, 19-32.

ANDO, M., 1974, Faulting in the Mikawa earthquake of 1945. *Tectonophysics*, **22**, 123-186.

FITCH, T. J. and C. H. SCHOLZ, 1971, Mechanism of underthrusting in Southwest Japan: A model of convergent plate interactions. *J. Geophys. Res.*, **76**, 7260-7292.

HASTIE, L. M. and J. C. SAVAGE, 1970, A dislocation model for the 1964 Alaska earthquake. *Bull. Seismol. Soc. Am.*, **60**, 1389-1392.

KANAMORI, H. and M. ANDO, 1973, Fault parameters of the great Kanto earthquake of 1923. In: *Publications for the 50th anniversary of the great Kanto earthquake, 1923*. Earthq. Res. Inst., Univ. Tokyo, 89-101.

LYSMER, J. and L. A. DRAKE, 1972, A finite element method for seismology. In: Bold, B. A. (editor), *Method in computational physics, Vol. 11, Seismology: surface waves and earty oscillation*. Academic Press, New York, 181-216.

MANSHINHA, L. and D. E. SMYLIE, 1971, The displacement field of inclined faults. *Bull. Seismol. Soc. Am.*, **61**, 1433-1440.

MARUYAMA, T., 1964, Static elastic dislocations in an infinite and semi-infinite medium. *Bull. Earthq. Res. Inst., Univ. Tokyo*, **42**, 289-368.

MCGARR, A., S. M. SPOTTISWOODE and N. C. GAY, 1975, Relationship of mine tremors to induced stresses and to rock properties in the focal region. *Bull. Seismol. Soc. Am.*, **65**, 981-993.

PLAKFER, G. and J. C. SAVAGE, 1970, Mechanism of the Chilean earthquakes of May 21 and 22, 1960. *Bull. Geol. Soc. Am.*, **81**, 1001-1030.

SAVAGE, J. C. and L. M. HASTIE, 1966, Surface deformation associated with dip-slip faulting. *J. Geophys. Res.*, **71**, 4897-4904.

SAVAGE, J. C. and L. M. HASTIE, 1969, A dislocation model for the fair-view peak Nevada earthquake. *Bull. Seismol. Soc. Am.*, **59**, 1937-1948.

SHIMAZAKI, K., 1974, Pre-seismic crustal deformation caused by an underthrusting oceanic plate, in eastern Hokkaido, Japan. *Phys. Earth Planet. Interiors*, **8**, 148-157.

STEPHANSON, O. and H. BERNER, 1971, The finite element method in tectonic processes. *Phys. Earth Planet. Interiors*, **4**, 301-321.

ZIENKIEWICZ, O. C., 1971, *The finite element method in engineering science.* McGraw-Hill, London.

---

13. 有限要素法を使って求めた断層形成に伴う地殻変形

地震研究所　笠　原　順　三

有限要素法を用いて，断層形成に伴う地殻変形を求めた．4つの傾斜角，即ち，垂直，45°，26.7°，水平，の場合を試みた．断層帯は低弾性率物質で構成されていると仮定した．断層に複双力源を分布させた．境界条件，断層帯の厚さ，断層の長さ，断層の深さの効果を調べ，地表変形を求めた．境界条件は表面変形の大きさに影響する．しかし，厚さ，長さ，深さは表面変形の大きさばかりでなく，そのパターンにも影響する．2つの例について，全体の変位分布，応力分布を示した．1945年三河地震 (M=7.1) について，地表変形計算値と観測値を比較することによって最適断層モデルを求めた．このモデルは安藤のモデルとよく一致している．
